

Using Lagrangian filtering to remove waves from the ocean surface velocity field

C. Spencer Jones^{1,2}, Qiyu Xiao³, Ryan P. Abernathey² and K. Shafer Smith³

¹Texas A&M University, College Station, TX

²Columbia University, New York, NY

³New York University, New York, NY

Key Points:

- We present a recipe for using Lagrangian filtering to filter waves from the ocean surface velocity field
- Removing super-inertial energy using Lagrangian filtering preserves some super-inertial energy in the Eulerian frame
- Preserved surface velocities are associated with convergent fronts, suggesting that Lagrangian filtering retains transport-active nongeostrophic flows

Corresponding author: C Spencer Jones, spencerjones@tamu.edu

14 Abstract

15 The Surface Water and Ocean Topography (SWOT) satellite will measure altimetry
 16 on scales down to about 15km: at these scales, the sea-surface-height signature of inertia-
 17 gravity waves, including barotropic tides and internal tides, will be visible. However, tides
 18 and inertia-gravity waves have little impact on tracer transport. Recent work has shown that
 19 Lagrangian filtering can be used to isolate the inertia-gravity wave part of the flow. This
 20 manuscript presents a recipe for removing barotropic motions and inertia-gravity waves from
 21 the surface velocities and from the sea surface height, to estimate the balanced part of the
 22 flow in the Agulhas region of a high-resolution ocean model (LLC4320). First, two methods
 23 for removing the barotropic component of sea surface height variability are presented. Then
 24 Lagrangian filtering, a method that accounts for Doppler shifting of high-frequency motions
 25 by the low-frequency velocity field, is applied to both the sea surface height and the ocean
 26 surface velocity field. The results of Lagrangian filtering are presented in spectral space.
 27 Lagrangian filtering preserves motions that appear super-inertial in the reference frame
 28 of the Earth, while other methods do not preserve these motions as effectively. In some
 29 locations most of the energy at high frequencies comes from these Doppler shifted balanced
 30 motions. We show that the balanced part of the velocity field that is preserved more
 31 effectively by Lagrangian filtering includes convergent motions near regions of frontogenesis.

32 Plain Language Summary

33 Scientists often want to divide up the velocity at the surface into two parts: the part
 34 of the velocity that transports ocean tracers (like heat, salt and carbon), and the wave-like
 35 part of the velocity that is irrelevant for ocean tracer transport. Lagrangian filtering is a
 36 recently discovered method for doing this: it accounts for how the ocean velocities change
 37 the frequency of some of the signals we measure through Doppler shift. In this paper, we
 38 provide a recipe for using Lagrangian filtering to find the non-wave part of the flow, and
 39 we compare Lagrangian filtering to alternative methods. Lagrangian filtering seems to do a
 40 better job of revealing the part of the ocean surface velocity that transports tracers.

41 1 Introduction

42 Near-surface ocean currents are a critical component of the Earth system, mediating
 43 the transfer of heat, momentum, and trace gasses between ocean and atmosphere (Cronin
 44 et al., 2019; Elipot & Wenegrat, 2021). These currents regulate marine ecosystems by
 45 transporting nutrients and phytoplankton laterally within the eutrophic zone (Barton et al.,
 46 2010; Resplandy et al., 2011) and transporting marine debris and plastic pollution around
 47 the globe (Van Sebille et al., 2020). Observed ocean surface currents are also used to
 48 evaluate the accuracy and biases of numerical ocean models. As a result, the oceanographic
 49 community requires accurate and detailed knowledge of the state of ocean surface currents.

50 Satellite-based observations of sea-surface height (SSH), which is directly proportional
 51 to surface pressure, can be used to infer surface velocities via geostrophic balance. Modern
 52 ocean altimetry products like Archiving, Validation, and Interpretation of Satellite Oceanographic
 53 data (AVISO) (Ducet et al., 2000) typically have grid resolution of around 0.25° and
 54 an effective resolution of approximately 200 km. At this scale, geostrophic balance holds
 55 well, and altimetry-derived near-surface geostrophic velocities are used in many studies
 56 of ocean currents (e.g., Niiler et al., 2003; Abernathey & Marshall, 2013; Mkhinini et al.,
 57 2014, and many others). Direct observations from drogued drifters, such as those from the
 58 NOAA Global Drifter Program, are an additional source of surface velocity data. While
 59 highly accurate, such measurements are relatively sparse, with approximately one drifter in
 60 every $5^\circ \times 5^\circ$ box of the ocean (Elipot et al., 2016).

61 The recently-launched Surface Water and Ocean Topography (SWOT) satellite will
 62 provide altimetry at scales down to $\sim 15\text{km}$ (Morrow et al., 2019). These measurements have
 63 the potential to greatly enhance our understanding of ocean surface currents, particularly at
 64 smaller scales. However, the SWOT measurements will also pose two distinct challenges for
 65 the estimation of velocities. First, the SWOT signal will presumably contain inertia-gravity
 66 waves (including internal tides), which have an imprint on both the SSH and the velocity field
 67 (Zaron & Rocha, 2018). Second, even if the waves were to be removed somehow, geostrophy
 68 becomes increasingly inaccurate at SWOT scales, where the Rossby number ($\text{Ro} = \tau/f$
 69 where τ is the advective timescale of the flow) gets closer to one and the nonlinear terms in
 70 the momentum equation become important (Callies et al., 2020).

71 In order to make progress on this problem, it is helpful to separate the internal tidal
 72 signal, as well as other non-tidal IGW components from the total SWOT SSH signal: this is
 73 a major focus of the SWOT science team research (Ponte et al., 2017; Lahaye et al., 2019;
 74 Klein et al., 2019). Some applications of near-surface velocities, particularly for the study
 75 of transport phenomena, benefit from a wave-free velocity field. The waves can indirectly
 76 influence tracer transport by modulating the energetics of the eddy field, but they make a
 77 minimal direct contribution to transport due to their quasi-linearity (Plumb, 1979; Balwada
 78 et al., 2018). Quasi-linear waves may displace tracer contours but don't cause these contours
 79 to fold or filament; nonlinear interactions are usually required to create small-scale tracer
 80 structures that enable mixing in the vertical. The barotropic tidal signal is already removed
 81 from conventional altimetric SSH as part of the data processing (Stammer et al., 2014).

82 Since SWOT will resolve smaller scales than previous altimeters, it will observe energetic
 83 eddies and fronts in which the Rossby number is order one. Thus even after the IGW signal
 84 has been filtered from the surface velocities and the SSH, the height field is unlikely to be in
 85 simple geostrophic balance with the velocity field. The remaining parts of the flow include
 86 higher-order balances such as gradient-wind and semi-geostrophy, but also the complex
 87 interactions between frontogenetic convergence and vertical mixing (e.g. turbulent thermal-
 88 wind balance) that don't really qualify as either balanced or wave motions. Still, we need
 89 language to describe these non-wave, non-geostrophic flows, so in lieu of a widely-accepted
 90 term, we refer to them here as “balanced ageostrophic” motions.

91 Both balanced geostrophic and balanced ageostrophic motions are likely to be important
 92 for transporting tracers in the horizontal, but because geostrophic motion is approximately
 93 non-divergent, balanced ageostrophic motions are probably the most important flows for
 94 transporting tracers from the surface across the base of the mixed layer (Ferrari, 2011; Lévy
 95 et al., 2018; Mahadevan et al., 2020; Uchida et al., 2020). Hence it is important not to
 96 accidentally remove balanced ageostrophic motions when removing IGWs from the SWOT
 97 SSH signal.

98 The combined challenges of filtering waves and retaining balanced ageostrophic motions
 99 mean that exploiting SWOT for inferring near-surface currents is far from trivial. Removing
 100 the IGW signal and studying the relationship between SSH and the balanced velocity field
 101 is a promising direction for future research. As a step towards estimating the balanced
 102 (transport-relevant) surface currents from SWOT data post launch, this paper investigates
 103 part 1 of the problem: how to accurately remove the IGW signal from near-surface ocean
 104 currents and preserve the transport-relevant part of the flow. We use a global eddy- and
 105 IGW-resolving GCM simulation, the MITgcm LLC4320. This simulation provides a realistic
 106 truth signal with much of the same complexity as the real ocean, including both IGWs and
 107 balanced ageostrophic motions.

108 Using this model, we compare and evaluate three different filtering methods for remov-
 109 ing IGWs and retaining the transport-relevant part of the surface velocity field. In doing
 110 so, we provide a recipe for estimating the balanced part of the flow. Each of these three
 111 methods has been used to remove or isolate IGWs in previous work, but the novelty of this
 112 paper is that we perform a detailed comparison of these methods at the ocean surface. The

113 first method applies a frequency-based filter at a fixed location, the second method applies
 114 a frequency-based filter along particle pathways, and the third method applies a frequency-
 115 wavenumber filter to a chosen region of the ocean. A perfect separation between balanced
 116 ageostrophic motions (the so-called ‘slow manifold’) and inertia-gravity waves (the so-called
 117 ‘fast manifold’) is likely to be impossible, because these categories are sometimes fuzzy. But
 118 there are significant differences between the three methods that suggest that some of them
 119 are more effective than others. Below, we provide some background about each of these
 120 methods.

121 It has long been known that most inertia-gravity waves have frequencies higher than the
 122 inertial frequency. One popular way of estimating the amount of energy in IGWs is to use a
 123 purely frequency-based method to isolate these motions. Furuichi et al. (2008); Richman et
 124 al. (2012) and Mazloff et al. (2020) all take a timeseries at each fixed physical location and
 125 apply a high-pass filter that preserves frequencies higher than the inertial frequency, before
 126 integrating over all frequencies to estimate the total energy in IGWs. A purely frequency-
 127 based method is also sometimes used to remove IGWs from the total velocity field. For
 128 example, Qiu et al. (2020) use a low-pass filter at each physical location to remove waves
 129 from their vertical velocity field. The first filtering method that we evaluate in this paper
 130 is purely Eulerian and frequency-based. Using this method, motions are measured at a
 131 fixed location on the Earth, with motions at frequencies lower than the inertial frequency
 132 labelled as balanced, and motions at frequencies higher than the inertial frequency labelled
 133 as wave-like.

134 Pinkel (2008), Shakespeare and Hogg (2017) and Caspar-Cohen et al. (2022) show
 135 that both balanced flows and IGWs are Doppler shifted by the large scale flow field. This
 136 means that fixed-location frequency filtering may be inaccurate, particularly in regions with
 137 fast background flows. Shakespeare and Hogg (2017) developed a method of filtering that
 138 accounts for this effect. Lagrangian particles are seeded in the horizontal flow field and record
 139 the velocity along their trajectories, i.e. in a flow-following coordinate system. Temporal
 140 (frequency) filtering is applied to the velocities recorded by each particle, after which the
 141 velocities are interpolated onto a regular grid. The second filtering method we use in this
 142 paper is Lagrangian filtering, based on the updated method by Shakespeare et al. (2021). In
 143 this method, motions are measured in flow-following coordinates, with motions at frequencies
 144 lower than the inertial frequency labelled as balanced and motions at frequencies higher than
 145 the inertial frequency are labelled as wave-like.

146 Torres et al. (2018) argue that instead of using a purely frequency-based method
 147 for identifying internal gravity waves, wavenumber information should also be used. Us-
 148 ing LLC4320 output for the Kurushio-Extension region, they plot the kinetic energy in
 149 frequency-wavenumber space. They find that at any given wavenumber, the energy at fre-
 150 quencies higher than the tenth baroclinic mode tends to fall along discrete beams aligned
 151 with the dispersion relation of each of the baroclinic modes. In their figures, the energy
 152 at frequencies below this curve tends to be continuously spread in frequency-wavenumber
 153 space, suggesting that it is associated with balanced motions. They subsequently estimate
 154 the amount of internal gravity wave energy in the model by integrating the energy at fre-
 155 quencies above the tenth baroclinic mode. The third filtering method in this paper labels
 156 motions with frequencies lower than the tenth baroclinic mode in frequency-wavenumber
 157 space as balanced, and motions with frequencies higher than the tenth baroclinic mode as
 158 wave-like.

159 This paper compares these three filtering methods: fixed-location frequency filtering
 160 (here called ω -filtering), Lagrangian filtering, and filtering frequencies higher than the tenth
 161 baroclinic mode (here called ω - k filtering). Our goal is to understand the differences between
 162 the three methods. We focus on Lagrangian filtering, which has not been substantially tested
 163 at the ocean surface.

164 Our results suggest that, in regions with strong mesoscale surface currents, Lagrangian
 165 filtering preserves a significant amount of horizontal flow that appears to be at super-inertial
 166 frequencies when measured at a fixed location. ω -filtering does not preserve these motions,
 167 and ω - k filtering only preserves some of these motions. We then examine the velocities that
 168 are preserved by Lagrangian filtering, to evaluate whether their properties are consistent
 169 with balanced flow. We use vorticity-strain joint probability-density functions to assess the
 170 effectiveness of each filtering method. Recent results from Balwada et al. (2021) show that
 171 fronts occupy a particular region of vorticity-strain space: if the filtered flow retains these
 172 features, then it is likely that fronts are being (correctly) categorized as balanced. We also
 173 examine the differences in the divergence field of the filtered velocities in physical space.

174 In addition to studying velocities, this paper examines how the three filtering methods
 175 affect sea surface height. Both balanced and wave motions have an impact on local sea
 176 surface height, so any filter that is applied to the surface velocity field may also be useful
 177 for separating balanced and wave flow signatures in the sea surface height field.

178 The three methods compared here are not the only possible methods for separating
 179 the balanced and wave-like parts of the flow. Other possible methods include linear and
 180 non-linear eigenvector methods (Kafiabad & Bartello, 2016; Chouksey et al., 2018; Eden
 181 et al., 2019), and methods that assume the potential vorticity is conserved and cannot
 182 be transferred to inertia-gravity waves (Viúdez & Dritschel, 2004; Masur & Oliver, 2020;
 183 Onuki, 2020). Most of these methods would require us to make significant assumptions
 184 about the initial condition, the lateral boundary conditions, the wind and other external
 185 forcing. However, they are useful for studying wave-mean interactions in models, and may
 186 be adapted to analyze LLC4320 data in the future.

187 Section 2 describes the region of LLC4320 used in this paper, together with the various
 188 methods used to filter the velocity and SSH fields: section 2.1 describes the removal of
 189 barotropic signals from the SSH and section 2.2 describes the different filtering methods
 190 used in this work. In section 3.1, we plot the frequency spectrum of horizontal velocity and
 191 SSH for the three filtering methods. Section 3.2 describes the frequency-wavenumber spectra
 192 of horizontal velocity for the three filtering methods. Section 3.3 and section 3.4 examine the
 193 properties of the velocities that are labeled as balanced by each filtering method, using joint
 194 probability density functions and the divergence combined with the frontogenesis function.
 195 A summary of our results and some conclusions are presented in section 4.

196 2 Methods

197 This study focuses on 75 days of SSH and velocity data taken from the Agulhas region
 198 of the LLC4320 simulation (Rocha et al., 2016), which is a $1/48^\circ$ global configuration of
 199 the MITgcm. The model includes tides, permits submesoscale variability and is able to
 200 resolve the IGW field at scales larger than 10km or so (Savage et al., 2017). The large data
 201 volume of the LLC4320 model, together with the large computational cost of the Lagrangian
 202 filtering method, compelled us to focus on a limited region of the ocean. This region was
 203 selected because of the presence of strong mesoscale flow features, including the Agulhas
 204 retroflection and the Antarctic Circumpolar Current. The chosen region, which is the same
 205 region used in Sinha et al. (2019), is shown in figure 1, and the time period extends from
 206 October to December 2011.

207 We compare several methods of partitioning the surface velocities, as detailed in section
 208 2.2. One of these methods requires the data to be transformed into frequency-wavenumber
 209 space. Because of the curvature of the globe and the presence of land in the domain, it is
 210 not possible to apply this transformation to the whole domain at once. Hence, we choose to
 211 compare filtering methods in two regions of the domain: region A (shown by the blue box
 212 in figure 1) and region B (shown by the green box in figure 1). Region A is chosen because
 213 it has a lot of energy in the inertia gravity wave field, whereas region B is chosen because

214 it has strong velocities at the mesoscale. Comparing these regions allows us to evaluate the
 215 differences between filtering methods in a region where IGWs are strong to one where they
 216 are relatively weak.

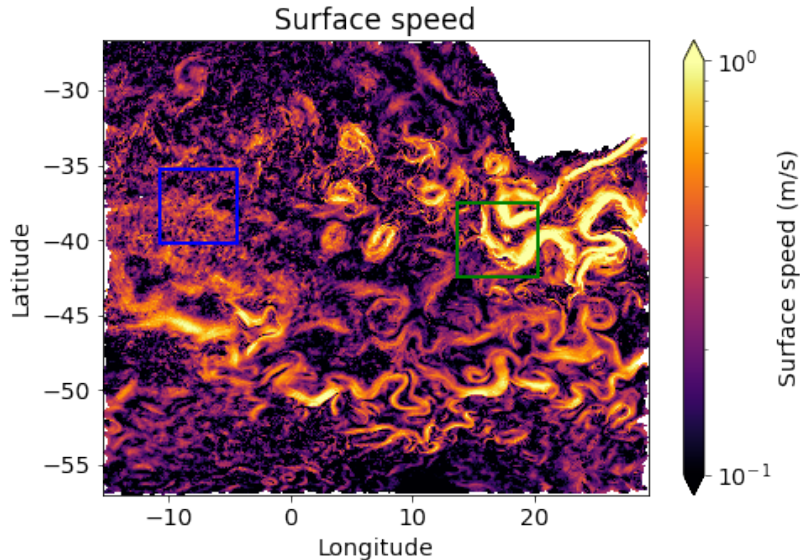


Figure 1. Snapshot of surface speed in our domain. The blue box is region A and the green box is region B. The white area in the north west of the domain is the southern part of Africa. The white areas around the edge indicate locations where seeded particles leave the domain within the 72 hour particle run.

217 **2.1 Removing the barotropic signal from the sea surface height**

218 The SSH contains variability that is associated with both balanced motions and with
 219 IGWs. However, it also contains a large amount of variability that is caused by barotropic
 220 motions, including the effects of barotropic tides, surface pressure changes and wind forcing.
 221 Because these barotropic motions have both subinertial and superinertial frequencies, the
 222 filtering methods described in section 2.2 are not designed to remove barotropic variability.
 223 Hence, we need to remove the barotropic part of the SSH variability before applying any
 224 other filtering method to the SSH field.

225 The tidal forcing of LLC4320 contains eight short-period tidal components, K_1 , O_1 ,
 226 P_1 , Q_1 , M_2 , S_2 , N_2 , and K_2 (Zhao et al., 2019), but LLC4320 has much more energy in
 227 the semidiurnal band than observations (Savage et al., 2017; Yu et al., 2019; Luecke et al.,
 228 2020). This is probably caused by the horizontal resolution, which resolves tidal forcing
 229 and propagation, but does not resolve the associated dissipative processes (Buijsman et al.,
 230 2020). Because of this difference from observations, an off-the-shelf tidal model tuned to
 231 the real ocean (e.g. the TPXO model, Egbert et al. (1994); Egbert and Erofeeva (2002)) is
 232 unlikely to be suitable for removing the barotropic tide from sea surface height in LLC4320.

233 Another common way to filter out the barotropic signal (including barotropic tides,
 234 pressure- and wind-forced barotropic variability) is to use the steric height. The total SSH,

235 η , is

$$236 \quad \eta(x, y, t) = \underbrace{\frac{p'_b(x, y, t)}{\rho_0 g} - \frac{p_a(x, y, t)}{\rho_0 g}}_{\text{non-steric}} - \underbrace{\int_{-H}^0 \frac{\rho'(x, y, z, t)}{\rho_0} dz}_{\text{steric}}, \quad (1)$$

237 from Wang et al. (2018), where H is the ocean depth, $p'_b = p_b - \rho_0 g H$ represents the bottom
 238 pressure anomaly, p_a is the atmospheric pressure, and the density $\rho = \rho_0 + \rho'(x, y, z, t)$.
 239 The steric component of SSH is controlled by baroclinic motions, including balanced flows,
 240 internal waves and internal tides. The non-steric component is controlled by barotropic
 241 motions including the barotropic tide.

242 Following Wang et al. (2018), we rearrange equation (1) to calculate the steric height
 243 from the total SSH, the atmospheric pressure and the bottom pressure:

$$244 \quad \eta_{\text{steric}} = \eta - \frac{p'_b}{\rho_0 g} + \frac{p_a}{\rho_0 g} \quad (2)$$

245 The power spectrum of the steric height is shown by the red dashed line in figure 2. In
 246 both region A and region B, the tidal peaks are much less prominent in the steric SSH than
 247 in the raw SSH (compare blue and red lines in figure 2). The steric height still retains a
 248 peak at M_2 and S_2 frequencies, because the semidiurnal tide forces IGW motions at these
 249 frequencies.

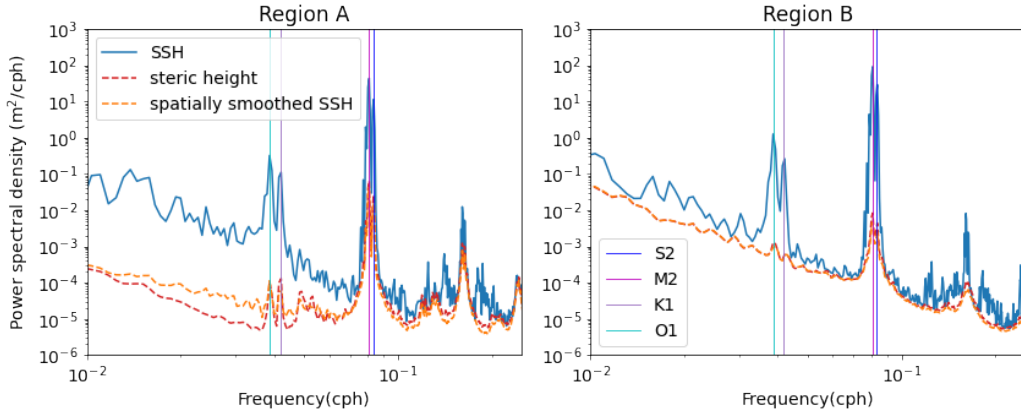


Figure 2. Power spectral density of the raw SSH (blue line), the steric height (red dashed line) and the SSH smoothed with a spatial filter (orange dashed line) in region A (left) and region B (right). Note that in region B the red dashed line is mostly obscured by the orange dashed line. Vertical lines mark the four highest-energy tidal frequencies, O_1 , K_1 , M_2 , S_2 .

250 Throughout the rest of this paper, whenever SSH is mentioned, the steric SSH is used.
 251 But we recognize that others may wish to apply our method to other kinds of data. If
 252 bottom pressure were not available, we could not calculate the steric height in this way.
 253 Because barotropic motions tend to have large spatial scales, we found that smoothing the
 254 SSH with a spatial filter (Grooms et al., 2021) that has a scale of 300km provides a good
 255 approximation of the steric height. The spectrum of the smoothed SSH is shown by the
 256 orange dashed line in figure 2.

2.2 Partitioning the wave and non-wave parts of the flow

2.2.1 ω -filtering

Frequency-based filtering, in which motions with frequencies lower than the inertial frequency are labelled as balanced and motions with frequencies higher than the inertial frequency are labelled as waves, is used as a baseline in this paper. This method has the main advantage of being very straightforward and computationally cheap. In our version of frequency filtering, we apply a convolution filter to the timeseries of velocity and steric SSH at each point in x, y, z . We choose to use a sinc function as the window function for this filter, because its Fourier transform is a top-hat (see e.g. Lilly and Lettvin (2004)), so the field after ω -filtering, ϕ_ω is given by

$$\phi_\omega(t) = \int_{t-t_w}^{t+t_w} \phi(t) \operatorname{sinc}\left(\frac{f(t-\tau)}{1.1\pi}\right) d\tau, \quad (3)$$

where ϕ is the unfiltered field and $t_w = 36$ hours. The width of the sinc function is chosen to be $f/1.1$, where f is the local Coriolis parameter. This width is chosen so that near-inertial waves, which have frequencies close to f , will be removed by the filter, in addition to other IGWs with frequencies above f . Although the Fourier transform of a sinc function is a top-hat, ω -filtering does not completely remove all of the energies at frequencies higher than the inertial frequency because the sinc function is only applied over a 72-hour window: it is a good but imperfect low-pass filter.

2.2.2 Lagrangian filtering

As described above, Lagrangian filtering is a method where the filter is applied to a timeseries collected at a location that moves with the horizontal flow field¹. Lagrangian filtering requires computing Lagrangian trajectories from the Eulerian velocity field. We accomplish this by using the MITgcm FLT package, together with offline mode, to compute particle trajectories from the velocity fields stored on disk (see Code Repository for numerical details of the configuration.) At time t_{init} , particles are seeded at every grid point. Each particle is run forwards in time with a timestep of 25s from time t_{init} for 36 hours, and u, v , and η_{steric} are recorded along the trajectory of the particle. Each particle is also run backwards in time from time t_{init} for 36 hours, and u, v , and η_{steric} are recorded along the trajectory of the particle. The forward and backward trajectories are concatenated to form a single 72 hour long trajectory, for which the midpoint is the position of the particle at time t_{init} . This reseeding method was designed by Shakespeare et al. (2021) to prevent the particles from clustering around regions of convergence, which would bias the spatial sampling of the particles.

We choose to use the same filter window for Lagrangian filtering as for ω -filtering. For Lagrangian filtering, the weighted average is taken for each 72-hour trajectory, with a new 72-hour trajectory generated every timestep, and then the weighted averages are concatenated in time, so the field after Lagrangian filtering, ϕ_{lf} is given by

$$\phi_{\text{lf}}(t = t_{\text{init}}) = \int_{-t_w}^{t_w} \phi_l(t_{\text{init}}, \tau) \operatorname{sinc}\left(\frac{f\tau}{1.1\pi}\right) d\tau, \quad (4)$$

where $\phi_l(t_{\text{init}}, \tau)$ is the property field measured along particle trajectories initiated at time t_{init} and τ is the time the property recorded by each particle relative to its initialization time t_{init} .

Just as for ω -filtering above, the filter is a sinc function with width $f/1.1$, where f is the local Coriolis parameter for the position of the particle at time t_{init} . Our chosen filter is

¹ Doppler shift has a negligible effect in the vertical direction (Shakespeare & Hogg, 2017), so horizontal advection of particles is sufficient.

much sharper than the Butterworth filter used by Shakespeare et al. (2021): this means that our method removes more energy from waves than the Shakespeare et al. (2021) method.

2.2.3 ω - k filtering

Torres et al. (2018) propose a method of partitioning the balanced flow and the wave flow along a contour in frequency-wavenumber space. This contour is the dispersion curve of the tenth baroclinic mode: for a given wavenumber, the first nine baroclinic modes are found at higher frequencies than this contour (see figure 3 of Torres et al. (2018)). Torres et al. (2018) categorize motions with frequencies above the contour as waves, and motions with frequencies below the contour as balanced flow. In this paper, we refer to this method as ω - k filtering.

To perform ω - k filtering, we must transform the data from physical space to frequency-wavenumber space. A multidimensional Fourier transform only makes sense when all the dimensions are orthogonal, so we first project the field $\phi(\text{lon}, \text{lat}, t)$ in regions A and B from the sphere onto a tangent plane that is parallel to the Earth's surface at the center of each region. We then apply a Tukey window and Fourier-transform the field $\phi(x, y, t)$ to get $\phi(k_x, k_y, \omega)$. Frequencies higher than the tenth baroclinic mode are set to zero, and an inverse-Fourier transform is applied to the result. We then divide by the Tukey window to compensate for the reduction in energy associated with windowing. Because the Tukey window goes to zero at the beginning and end of the timeseries, and along the edges of the domain, in these regions, the results of ω - k filtering are very noisy. We chose to use a Tukey window because it has a large flat region across the center of the domain, in which windowing does not generate noise.

Because of the need to project onto a tangent plane, and the necessity of windowing, ω - k filtering is not well-suited for estimating the balanced flow over a large region of physical space. It is more suitable for application to small regions. Torres et al. (2018) use ω - k filtering to calculate the balanced and wave energy in frequency-wavenumber space for small regions of physical space, without attempting to inverse-transform back to physical space.

3 Results

3.1 Frequency spectrum

The power spectra described here were calculated from a two-week-long dataset of the filtered and unfiltered fields at hourly resolution. For Lagrangian filtering, the filtering occurs in Lagrangian space, but the filtered velocities are transformed into Eulerian space before the spectrum is calculated. For all of the spectra, the unfiltered and filtered velocities are first averaged onto cell centers, and projected onto a tangent plane: this allows the results to be more easily compared with the frequency-wavenumber diagrams in section 3.2. The unfiltered, ω -filtered and Lagrangian filtered velocities are then used to calculate a power spectrum of speed, using all the points in each region. For ω - k filtering, the power spectrum is first calculated in frequency-wavenumber space, the filter is applied, and the result is summed over all wavenumbers to calculate the power spectrum as a function of frequency only.

The power spectrum of the horizontal speed in all three methods is shown in the top two panels of figure 3². In region A, the unfiltered horizontal velocity field (the orange line

² We also computed rotary spectra, which reveal the difference between clockwise and counter-clockwise rotating flows, highlighting inertial oscillations. In these plots, for simplicity of presentation, we choose to focus just on the full spectrum, which is the sum of the clockwise and counter-clockwise components of the rotary spectrum.

343 in figure 3a) has a spectral peak at the inertial frequency (shown by the vertical black line
 344 in figure 3) and at the semidiurnal frequency (shown by the vertical blue line in figure 3), as
 345 well as additional peaks at various supertidal frequencies. These peaks are a feature of high-
 346 resolution global models, perhaps caused by insufficient resolution of internal wave triads
 347 (Savage et al., 2017; Arbic et al., 2022). These peaks are associated with inertia-gravity
 348 waves in LLC4320 (Torres et al., 2018).

349 Overall, there is more energy at high frequencies in region B than in region A. In region
 350 B, the spectrum of the unfiltered horizontal velocity has a small peak at the semidiurnal
 351 frequency, but does not have other peaks at higher tidal frequencies (orange line in figure
 352 3b). The spectrum of unfiltered steric SSH also has smaller peaks in region B than in region
 353 A (compare the orange lines in figure 3c and figure 3d). This suggests that a larger fraction
 354 of the total energy in region A is in IGWs.

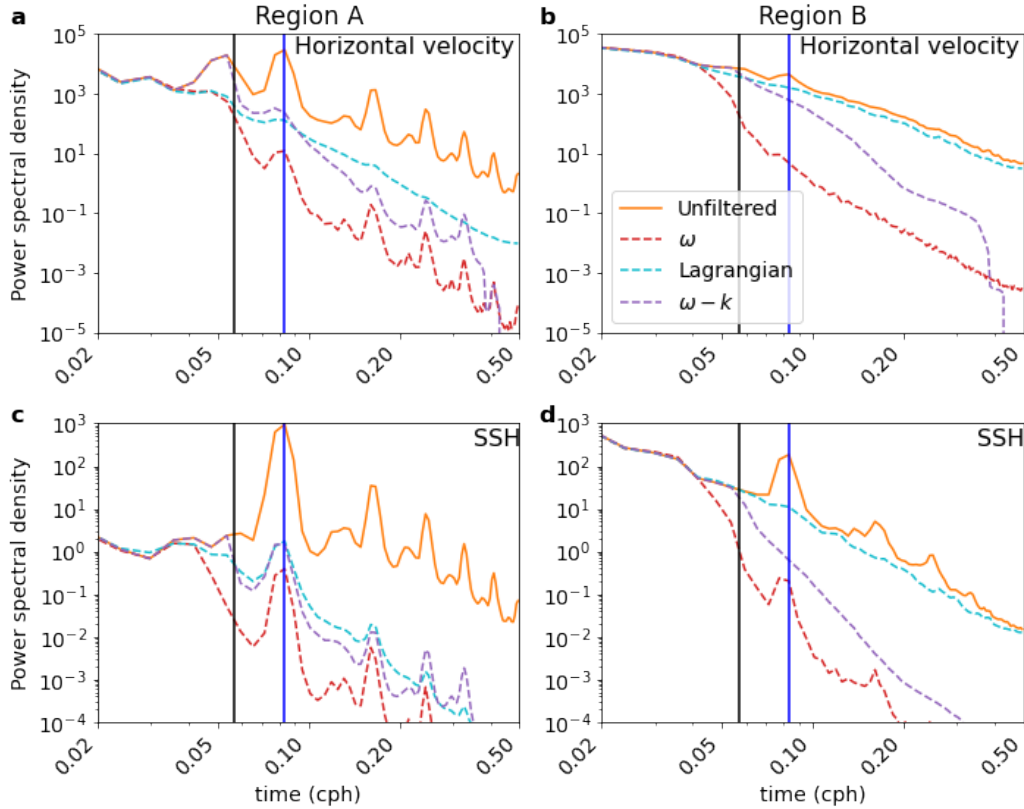


Figure 3. a) Power spectrum of horizontal velocity field calculated from the flow in region A, and b) power spectrum of horizontal velocity field calculated from the flow in region B. c) Power spectrum of SSH field calculated from the flow in region A and d) power spectrum of horizontal velocity field calculated from the flow in region B. In each panel, the orange solid line is the spectrum of the unfiltered field, the red dashed line is the spectrum of the ω -filtered field, the cyan dashed line is the spectrum of the Lagrangian filtered field and the purple dashed line is the spectrum of the ω - k filtered field. The vertical black line is the inertial frequency and the vertical blue line is the semidiurnal frequency.

355 In both regions, all three filtering methods reduce the high frequency energy of the
 356 horizontal velocity field, but ω -filtering removes the most energy from these frequencies

(red dashed line in all panels of figure 3). Although they use exactly the same window function in their filter, there is a significant difference between ω -filtering and Lagrangian filtering. In fact at higher frequencies, Lagrangian filtering retains the most superinertial energy of all the filtering methods. Recall that the spectra presented here were calculated in Eulerian space. Apparently high-frequency energy is retained by Lagrangian filtering because it is subinertial in Lagrangian space, but has been Doppler shifted and appears to be superinertial in Eulerian space. The logarithmic scale and high energy of the flow at subinertial frequencies means small differences in the subinertial energy are not visible in this figure: it is possible that an equal amount of energy that appears subinertial in the reference frame of the Earth but is superinertial in the reference frame of the flow is removed by Lagrangian filtering. This is explored further in section 3.2.

The ω - k -filtered spectrum retains more energy at subinertial frequencies than other methods, because the filter only removes frequencies higher than the 10th baroclinic mode. The roll-off of the ω -filter and Lagrangian filter are specifically designed to remove waves with intrinsic frequencies close to f , because we do not expect near-inertial waves to contribute to tracer transport.

In region A, the spectrum of the Lagrangian-filtered horizontal velocity has none of the peaks that are associated with IGWs in LLC4320, and only a small peak at the inertial frequency (cyan line in figure 3a). One interpretation of this result is that Lagrangian filtering is removing the IGW energy in the horizontal velocity field, including the energy concentrated at the tidal harmonics. ω - k filtering removes less energy than ω -filtering, but it still reduces the energy at high frequencies by more than an order of magnitude (purple dashed line in figure 3b). Lagrangian filtering also removes the tidal peaks in the unfiltered SSH spectrum in region B (cyan line in figure 3d), but most of the high-frequency energy in the velocity field is retained (cyan line in figure 3b). One potential explanation is that Lagrangian filtering is mostly removing IGW energy in the SSH field in region B, but that most of the superinertial energy in region B comes from low-frequency motions that have been Doppler shifted into the superinertial range.

3.2 Frequency-wavenumber spectra

The frequency spectrum summarizes a lot of information about the flow, but to better understand the characteristics of each of the filtering methods, it is helpful to calculate the power spectrum in frequency-wavenumber space. Figure 4 shows the isotropic frequency-wavenumber diagram for the surface velocity in region A and figure 5 shows the same analysis for region B. The unfiltered velocities (figures 4a and 5a) contain more low-frequency energy in region B. In region A, the energy at frequencies higher than the 10th baroclinic mode (shown by the green contour) is concentrated in discrete bands, which suggests that this energy is associated with IGWs. In region B, the most of the energy at frequencies higher than the 10th baroclinic mode is smoothly connected to the energy at lower frequencies.

It is important to remember that these frequency-wavenumber diagrams are a representation of the amount of energy at each frequency and wavenumber measured in Eulerian space (regardless of what kind of filtering is applied). It is not feasible to calculate a frequency-wavenumber diagram in Lagrangian space, so the Lagrangian-filtered velocities are operated on in Eulerian space to create this diagram.

As expected, ω -filtering removes most of the energy at frequencies higher than the inertial frequency (figures 4b and 5b). However, Lagrangian filtering preserves a lot of energy with frequencies higher than the inertial frequency in the Eulerian frame. Lagrangian filtering is designed to remove energy at frequencies above the inertial frequency in a coordinate following the flow. Hence, energy that remains after Lagrangian filtering must be at subinertial frequencies in the Lagrangian frame, and must be Doppler-shifted into the superinertial range by velocities that change on longer timescales. The energy that is preserved by Lagrangian filtering generally has large wavenumbers.

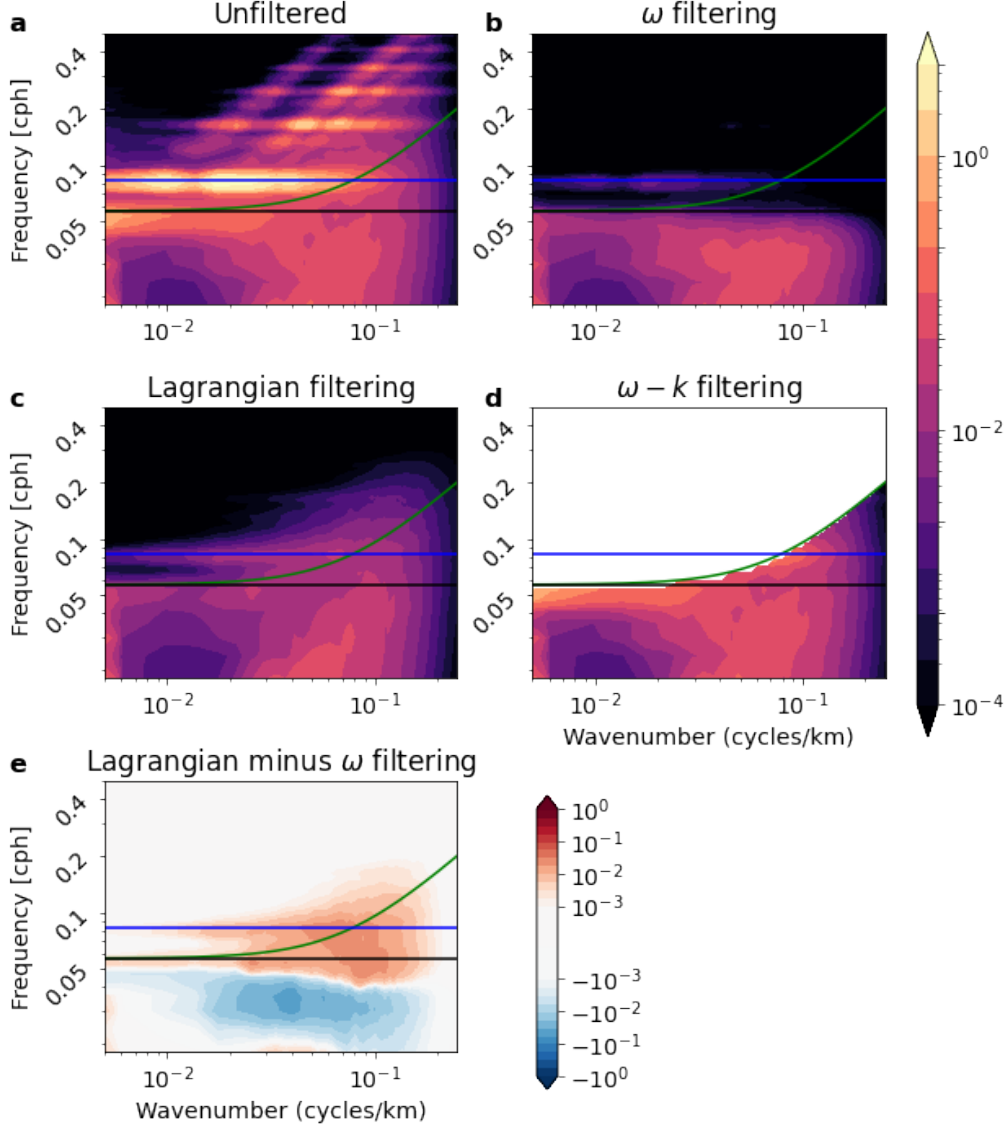


Figure 4. The isotropic frequency-wavenumber spectrum of horizontal velocity field calculated from the flow inside region A, the blue box of figure 1, for a) the unfiltered velocity field, b) the ω -filtered velocity, c) the Lagrangian filtered velocity and d) the ω - k filtered velocity. e) The frequency-wavenumber spectrum of Lagrangian filtered horizontal velocity minus the frequency-wavenumber spectrum of the ω -filtered velocity. The black horizontal line is the inertial frequency and the blue horizontal line is the semidiurnal frequency. The green line is the tenth baroclinic mode. The isotropic frequency-wavenumber spectrum is obtained by azimuthally-averaging over all values of k , where $k = \sqrt{k_x^2 + k_y^2}$.

408 The figures 4e and 5e show the difference between the frequency-wavenumber spectrum
 409 with Lagrangian filtering and the frequency-wavenumber spectrum with ω -filtering. In both
 410 regions, the Lagrangian-filtered velocities have more energy at superinertial frequencies in
 411 the Eulerian frame and less energy at subinertial frequencies in the Eulerian frame. This
 412 indicates that Doppler shifting is likely happening in both directions: ω -filtering spuriously

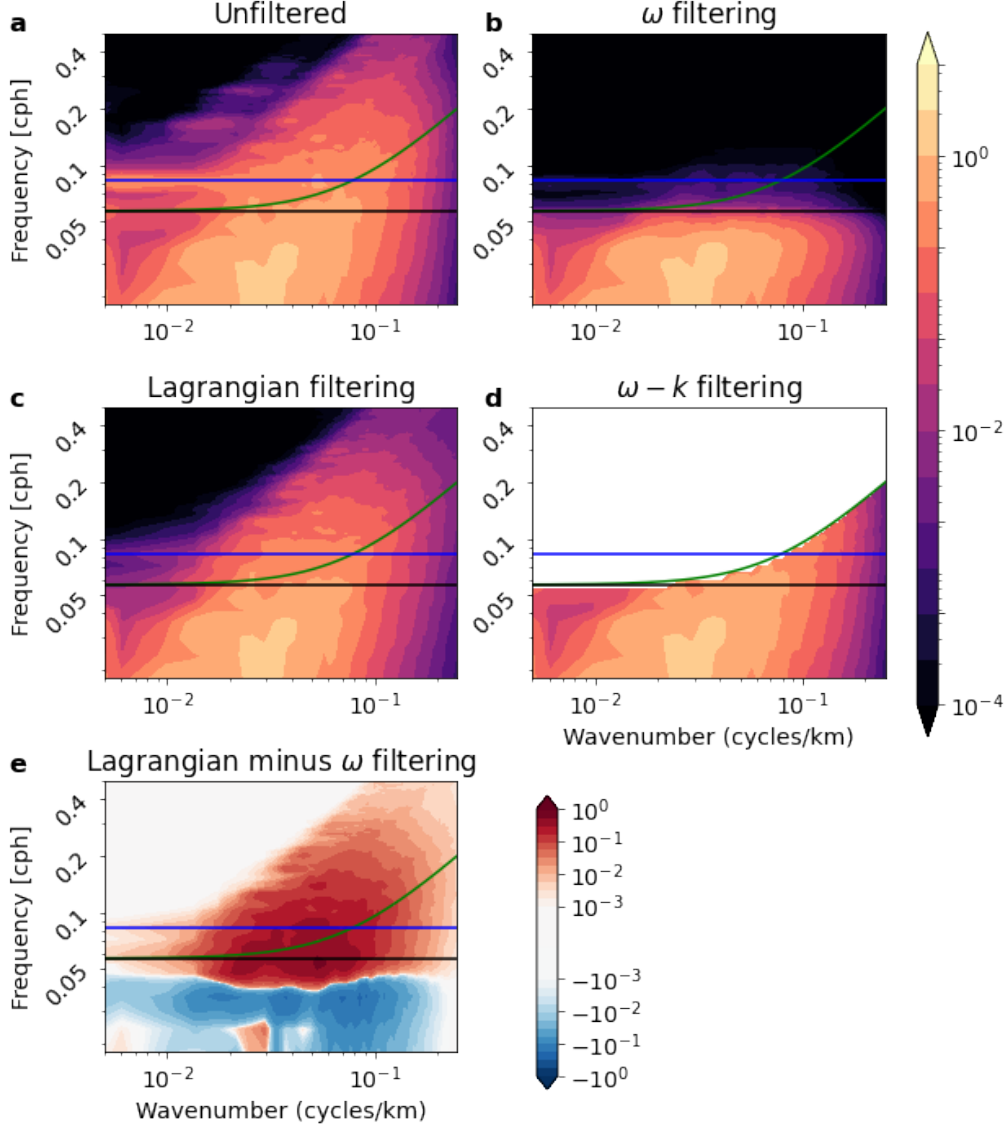


Figure 5. The isotropic frequency-wavenumber spectrum of horizontal velocity field calculated from the flow inside region B, the green box of figure 1, for a) the unfiltered velocity field, b) the ω -filtered velocity, c) the Lagrangian filtered velocity and d) the ω - k filtered velocity. e) The frequency-wavenumber spectrum of Lagrangian filtered horizontal velocity minus the frequency-wavenumber spectrum of the ω -filtered velocity. The black horizontal line is the inertial frequency and the blue horizontal line is the semidiurnal frequency. The green line is the tenth baroclinic mode. The isotropic frequency-wavenumber spectrum is obtained by azimuthally-averaging over all values of k , where $k = \sqrt{k_x^2 + k_y^2}$.

413 removes flow that is Doppler shifted into the superinertial range, and spuriously retains flow
 414 that is Doppler shifted into the subinertial range.

415 The frequency-wavenumber diagram after ω - k filtering is shown in the figures 4d and
 416 5d for comparison with Lagrangian filtering. ω - k filtering removes a large amount of

417 super-inertial energy in both region A and region B. However, much more of the low- to
 418 intermediate-wavenumber super-inertial energy in region B is retained by Lagrangian fil-
 419 tering, suggesting that much of this energy is associated with balanced flow that has been
 420 Doppler-shifted into the super-inertial range. Region B is characterized by stronger currents,
 421 so more pronounced Doppler shift is expected.

422 3.3 Vorticity-strain JPDFs

423 One way to evaluate the separation of wave velocity and balanced velocity is by consid-
 424 ering the joint probability density function (JPDF) of the normalized-by- f surface vorticity
 425 ζ/f , strain $\sigma/|f|$, and divergence δ/f , where

$$426 \quad \zeta = v_x - u_y \quad (5)$$

$$427 \quad \sigma = \sqrt{(u_x - v_y)^2 + (v_x + u_y)^2} \quad (6)$$

$$428 \quad \delta = u_x + v_y. \quad (7)$$

430 Balwada et al. (2021) found that the vorticity-strain JPDFs of submesoscale-rich flows are
 431 characterized by a clear frontal signature, appearing as concentrations along the ± 1 slope
 432 lines, because $|\zeta| \approx \sigma$ for fronts. Moreover, because large frontal vertical velocities generate
 433 vortex stretching in the vorticity equation, submesoscale fronts are highly asymmetric and
 434 skewed toward positive vorticity, which appears as a long tail on the cyclonic side of the
 435 JPDF. By contrast, wave-dominated super-inertial flows tend to have $|\zeta| \ll |\delta| \sim \sigma$ and
 436 lack an asymmetry-generating mechanism, and thus have vorticity-strain JPDFs that are
 437 mostly symmetric and centered around the origin³. Thus by considering the vorticity-strain
 438 JPDFs calculated from the filtered and unfiltered velocity fields, we can get a sense of how
 439 well the various filtering methods preserve frontal features and remove waves.

440 Figure 6 shows, for regions A and B, the vorticity-strain JPDFs of the unfiltered velocity,
 441 the ω -filtered velocity, the Lagrangian-filtered velocity, and the unfiltered-minus-filtered
 442 velocity fields for each filtering method (specifically, we compute the JPDFs of the velocity
 443 field obtained by subtracting the filtered from the unfiltered velocity). The unfiltered-minus-
 444 filtered velocity fields represents the IGW part as inferred by each method. The JPDF of
 445 the unfiltered velocity is more asymmetric and extends much farther along the $\zeta = \sigma$ line in
 446 region B than in region A, consistent with the former being characterized by higher energy
 447 and more submesoscale fronts (compare the panels in the top row of figure 6). The JPDFs of
 448 the unfiltered velocity fields for each region share roughly the same shapes with their filtered
 449 velocity fields, using any filtering method, indicating that both the filtered and unfiltered
 450 velocity fields contain some balanced flows associated with fronts.

451 The JPDFs of the unfiltered-minus-filtered velocities (i.e. the velocities categorized as
 452 waves) are different between filtering methods. In region A, the JPDFs are relatively sym-
 453 metric, indicating that a few submesoscale fronts are mis-categorized as wave-like. However,
 454 in region B, the JPDF of the unfiltered-minus-filtered flow are asymmetric for ω -filtering and
 455 ω - k filtering, but symmetric with Lagrangian-filtering. This suggests that, at least in region
 456 B, where balanced ageostrophic flows are strong, ω -filtering and ω - k filtering spuriously
 457 filters out parts of balanced flow (mis-categorizing them as wave-like), while Lagrangian
 458 filtering does not. Moreover, in both regions, ω -filtering removes larger vorticity and strain
 459 values, while Lagrangian-filtering preserves them. These JPDFs provide additional evi-
 460 dence that in both regions, Lagrangian filtering is more effective at removing waves, while
 461 preserving balanced ageostrophic flows, than ω -filtering.

³ Consider, for example, a shallow water inertia-gravity wave, which has $\zeta = f|\mathbf{k}|/\omega \cos \theta$ and $\delta = |\mathbf{k}| \sin \theta$, where \mathbf{k} is the horizontal wavenumber and $\theta = \mathbf{k} \cdot \mathbf{x} - \omega t$. Thus $\zeta/\delta \sim f/\omega$, so that for high-frequency waves, $|\zeta| \ll |\delta|$. Moreover, $\sigma = \sqrt{\zeta^2 + \delta^2}$, so for high-frequency waves, $\sigma \sim |\delta|$.

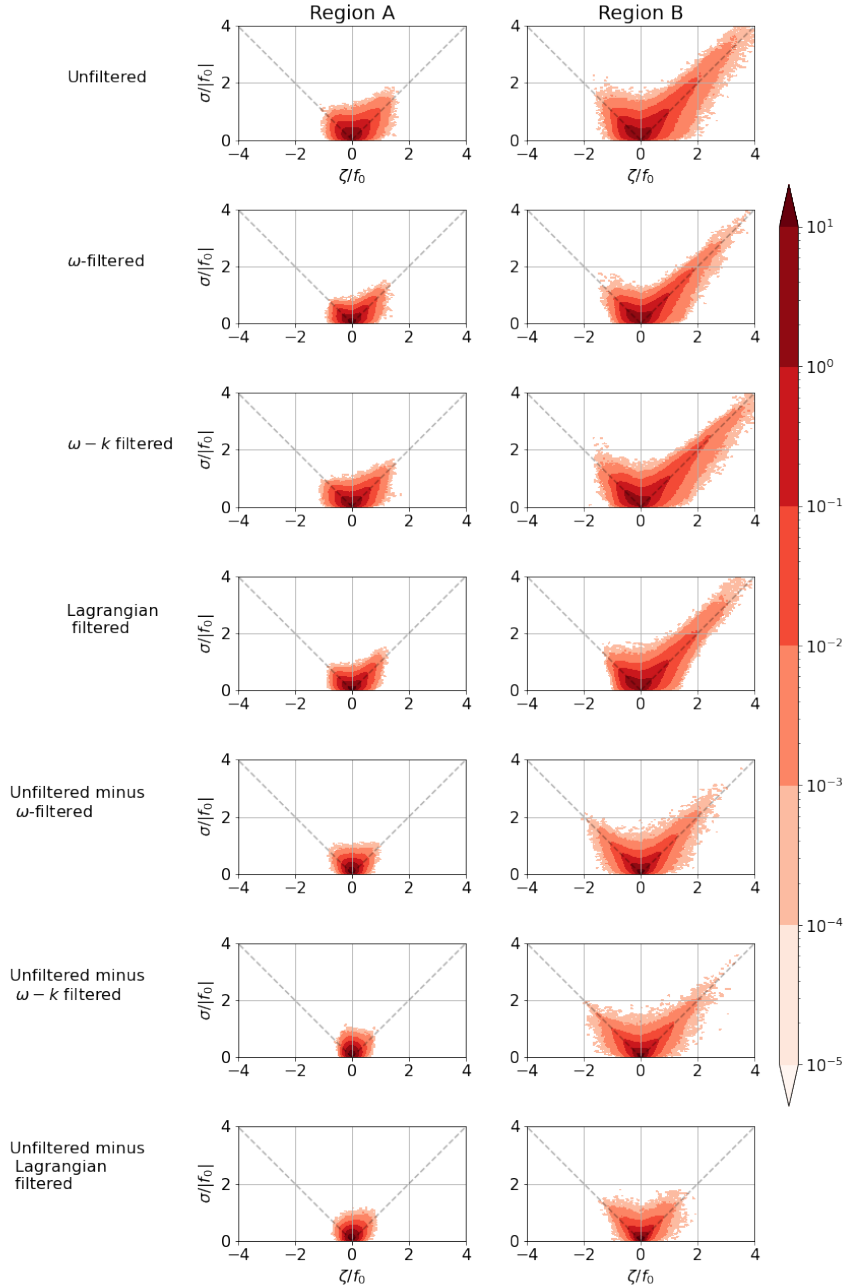


Figure 6. Vorticity-strain joint probability density functions calculated from surface velocities in region A (left) and in region B (right). The dashed lines are the $|\zeta| = \sigma$ lines: submesoscale fronts tend to be concentrated just above the cyclonic $\zeta = \sigma$ line (Balwada et al., 2021). For the ω - k filtered velocities are projected onto a tangent plane before the JPDF is calculated, but all other JPDFs are calculated without projection (projection onto a tangent plane introduces a small error in the vorticity and strain fields).

462

3.4 Divergence in physical space

463

464

The horizontal velocities associated with waves are more divergent than the horizontal velocities associated with geostrophically-balanced flows (see e.g. Bühler et al. (2014)).

465 However, upper-ocean submesoscale flows are characterized by strongly convergent fronts.
 466 An important test of filtering methods is the degree to which they retain the divergence
 467 associated with submesoscale fronts while removing the divergence associated with wave-
 468 like flows. We show the divergence of the surface velocity field for a representative time
 469 snapshot in figure 7 (region A) and in figure 8 (region B). We also plot the frontogenesis
 470 function,

$$471 \quad F_s = \mathbf{Q}_s \cdot \nabla_h b, \quad (8)$$

472 where $\mathbf{Q}_s = -\left(\frac{\partial u}{\partial x} \frac{\partial b}{\partial x} + \frac{\partial v}{\partial x} \frac{\partial b}{\partial y} + \frac{\partial w}{\partial x} \frac{\partial b}{\partial z}, \frac{\partial u}{\partial y} \frac{\partial b}{\partial x} + \frac{\partial v}{\partial y} \frac{\partial b}{\partial y} + \frac{\partial w}{\partial y} \frac{\partial b}{\partial z}\right)$. Large positive values indi-
 473 cate that the flow field is acting to increase the buoyancy gradient (Hoskins, 1982; Capet et
 474 al., 2008; Brannigan et al., 2015). Hence, these large values tend to be present at fronts.

475 Here, we compare the divergence field with the frontogenesis function: we expect that
 476 regions with high convergence associated with fronts will be associated with high values of
 477 the frontogenesis function. Of course, the frontogenesis function may not be high for all
 478 balanced convergent or divergent features, and not all such features are necessarily fronts.

479 Figures 7 and 8 show that ω -filtering, Lagrangian filtering and ω - k filtering all reduce the
 480 divergence of the velocity field significantly. In region A, ω -filtering and Lagrangian filtering
 481 reduce the divergence more than ω - k filtering (compare figure 7b, c, and d with figure 7a),
 482 even in regions with a low frontogenesis function. This suggests that ω - k filtering does not
 483 remove all the waves. Both ω -filtering and Lagrangian filtering preserve higher divergences
 484 and convergences close to regions where the frontogenesis function is large and positive (the
 485 region surrounded by a thin black contour). Figures 7e,f and 8e,f show magnified parts of
 486 regions A and B where this effect is visible.

487 In region B, ω -filtering reduces the divergence the most out of all the filtering methods
 488 (Figure 8b). Lagrangian filtering preserves much more negative divergences in the region
 489 where the frontogenesis function is large and positive (Figure 8c,e,f). This suggests that in
 490 region B, Lagrangian filtering preserves more of the ageostrophically-balanced flow associ-
 491 ated with convergent fronts.

492 3.5 Geostrophy

493 Across most of the ocean, surface velocities that are estimated by applying geostrophy
 494 to the unfiltered sea-surface height field are not good predictors of the true sea-surface
 495 velocity field (Yu et al., 2021). Removing the inertia gravity wave signal removes velocities
 496 that are not in geostrophic balance, so we might expect that the filtered velocities will be
 497 more geostrophic than the unfiltered velocities. In figure 9, we estimate the geostrophic
 498 velocity by naively applying the geostrophic equation to the sea-surface-height field, and
 499 then take the root-mean-square difference between the surface speed and this SSH-derived
 500 geostrophic speed estimate:

$$501 \quad \text{RMS}^{ij} = \frac{1}{A} \int \sqrt{\frac{\left(\frac{1}{T} \int (|\mathbf{v}^i| - |\mathbf{v}_{\text{ssh}}^j|)^2 dt\right)}{\sigma_t(|\mathbf{v}^i|)}} dA, \quad (9)$$

502 where \mathbf{v} is the velocity at the surface, i is the type of filtering used on the velocity field (no
 503 filtering, ω -filtering, Lagrangian filtering or ω - k filtering), \mathbf{v}_{ssh} is the SSH-derived velocity
 504 field, j is the type of filtering used on the SSH field, and T is the total length of the
 505 timeseries after filtering (70days). We normalize this root-mean-square difference by the
 506 pointwise standard deviation of the velocity field, $\sigma_t(|\mathbf{v}^i|)$.

507 The raw-SSH-derived geostrophic velocity field is based on the unfiltered steric SSH,
 508 so it contains a significant amount of variability from waves. Applying a filter to the SSH
 509 before creating the SSH-derived geostrophic velocity estimates leads to marginally better
 510 agreement between the velocity field and the SSH-derived velocity field in region A (compare
 511 bottom row of the left panel of figure 9 with earlier rows). This suggests that the SSH is

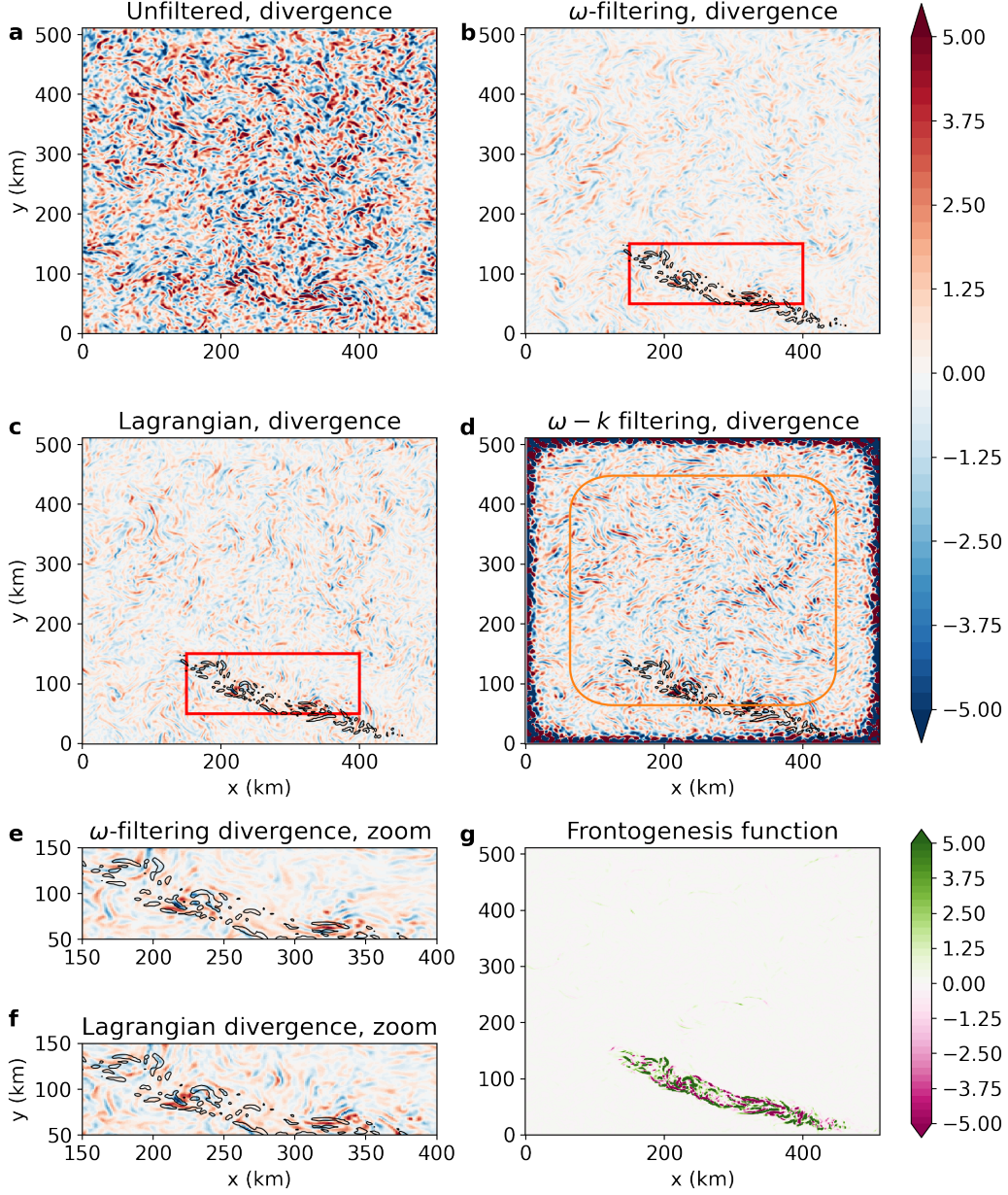


Figure 7. a-d) Divergence ($\times 10^5 \text{s}^{-1}$) of unfiltered and filtered velocities on day 35 in region A, the blue box of figure 1, e-f) the same quantities in the region inside the red box of b) and c) and g) the frontogenesis function ($\times 10^{14} \text{kg}^2/\text{m}^8/\text{s}$). Thin black contours show the 0.2 contour of the frontogenesis function. Inside the orange contour, the window function used in $\omega - k$ filtering is greater than 0.5: inside this contour, inaccuracies due to windowing should be negligible.

512 strongly influenced by high frequency motions which are not geostrophic. Even though
 513 Lagrangian filtering may preserve more of the balanced flow at high frequencies, Lagrangian
 514 filtering is no better than ω -filtering for picking out geostrophic balance in region A. Hence,
 515 the high frequency flow that is preserved by Lagrangian filtering is mostly not in geostrophic
 516 balance.

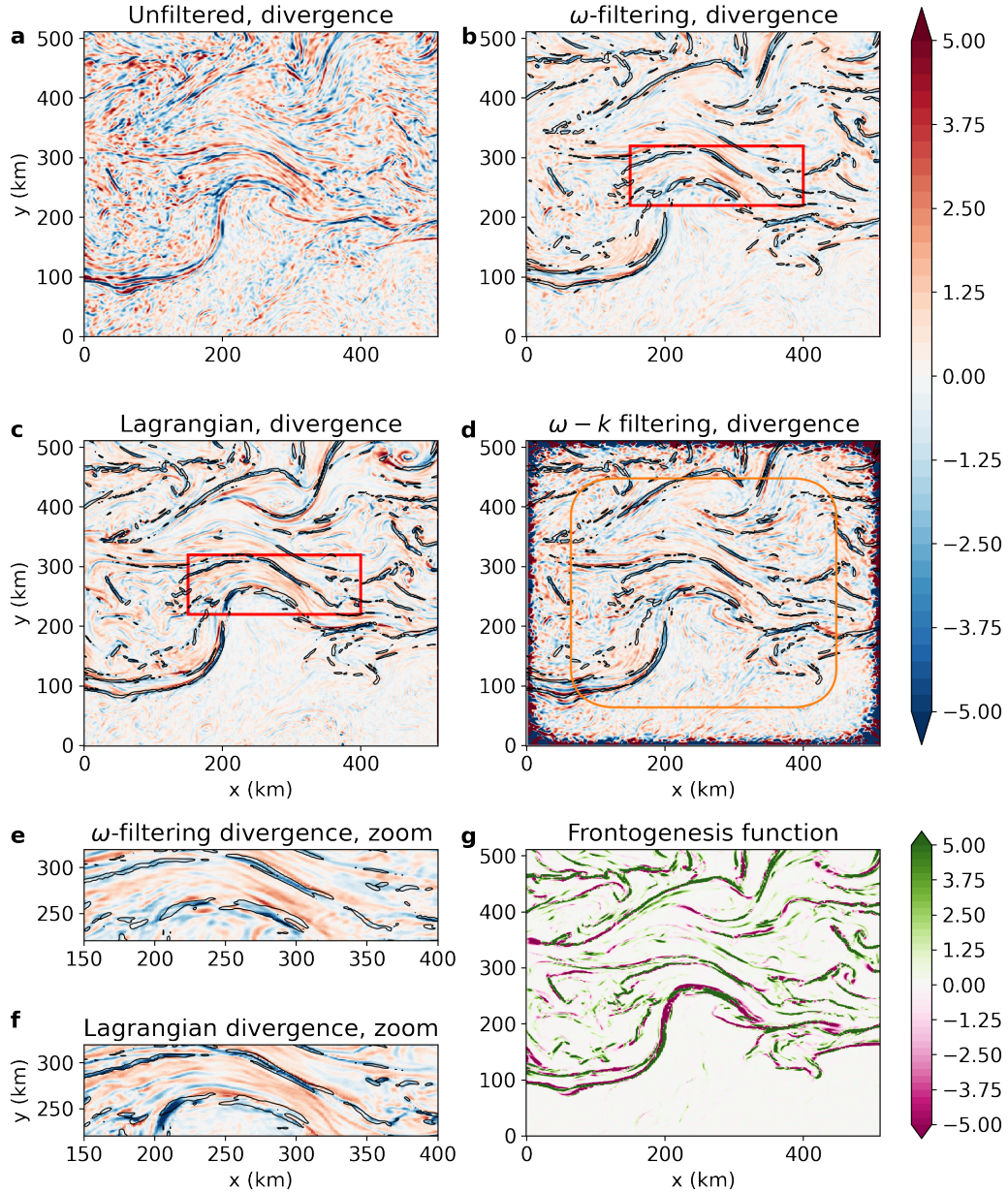


Figure 8. a-d) Divergence ($\times 10^5 \text{ s}^{-1}$) of unfiltered and filtered velocities on day 35 inside the green box of figure 1, e-f) the same quantities in the region inside the red box of b) and c) and g) the frontogenesis function ($\times 10^{14} \text{ kg}^2/\text{m}^8/\text{s}$). Black contours show the 1 contour of the frontogenesis function. Inside the orange contour, the window function used in ω - k filtering is greater than 0.5: inside this contour, inaccuracies due to windowing should be negligible.

517 In region B, filtering the velocity field does not significantly improve its agreement
 518 with the raw-SSH-derived geostrophic velocity estimate (bottom row of right panel in figure
 519 9). This is probably because region B contains a lot of submesoscale activity and most of
 520 the balanced flows in region B are ageostrophic. Applying an ω -filter or ω - k filter to the
 521 SSH field leads to more agreement between SSH-derived velocity estimate and the surface
 522 velocities: both of these filters remove high frequency motions of all kinds from the SSH

523 field. Applying a Lagrangian filter to the SSH is generally less effective at picking out
 524 geostrophy, suggesting that a lot of the motion preserved by Lagrangian filtering in region
 525 B is not geostrophic (even if it is balanced).

526 Regions A and B are in two very different regimes, but geostrophy is not an effective way
 527 to calculate surface velocities from sea-surface height in either regime. Applying geostrophic
 528 balance to SWOT measurements at small scales is unlikely to be an effective way to calculate
 529 ocean surface velocities, even after filtering is applied. This is an important difference from
 530 previous satellite altimetry missions.

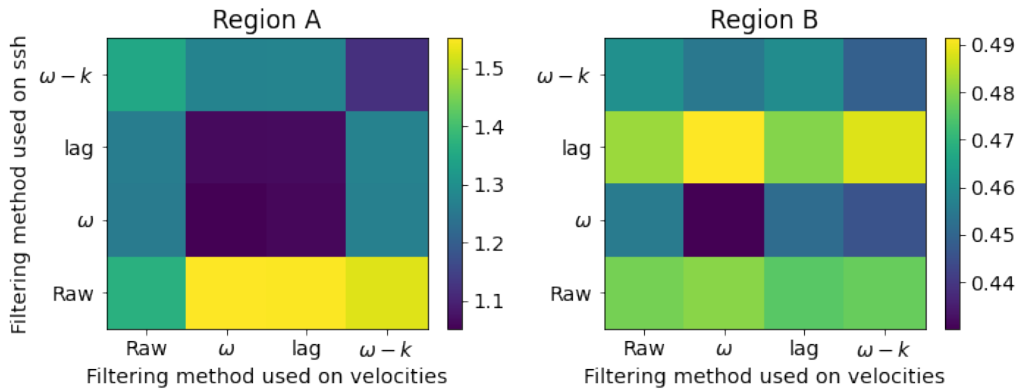


Figure 9. Normalized root mean square difference (RMS^{ij} in equation (9)) between the unfiltered surface speed and the surface speed calculated by applying the geostrophic equation to sea-surface height for the blue box of figure 1 (left) and the green box of figure 1 (right).

531 4 Conclusions

532 SWOT offers an unprecedented opportunity to observe the global sea surface height
 533 down to scales of $O(10 \text{ km})$, an order of magnitude improvement over the current generation
 534 of altimeters (Fu and Ferrari, 2008). While at coarser scales, geostrophic balance allows
 535 accurate estimation of upper-ocean velocity from SSH, no such simple balance can be used
 536 to extract velocities from SWOT measurements. The lack of a simple balance to relate SSH
 537 to velocities poses not only a challenge to determining the latter, it also implies that the
 538 velocity field itself is more complex at these scales. In particular, it will contain components
 539 due to both ageostrophic balances, as well as inertia-gravity wave signals. The latter do
 540 not impact tracer transport, but act as noise that complicates studies of the relationship
 541 between the SSH and the transport-relevant velocity field.

542 Here we have investigated an approach to solving one part of the complex puzzle posed
 543 by SWOT data: filtering wave signals from high-resolution data. The methods considered
 544 include simple low-pass filtering in frequency (termed ω -filtering), combined wavenumber-
 545 frequency filtering (ω - k filtering, after Torres et al. (2018)), and Lagrangian filtering (after
 546 Shakespeare and Hogg (2017); Shakespeare et al. (2021)).

547 ω -filtering is computationally very cheap, and it removes all motions at frequencies
 548 higher than f in the Eulerian frame from the surface velocity field. However, this process
 549 removes some motions that have been Doppler shifted to higher frequencies, including some
 550 motions associated with fronts and filaments. ω - k filtering, which was proposed by Torres
 551 et al. (2018), was designed based on the frequency-wavenumber properties of flow in the
 552 Kuroshio Extension region. Frequencies higher than the tenth baroclinic mode were ob-

served to fall in discrete bands, suggesting they were associated with IGWs. This paper shows that in region B (a region with strong mesoscale flows), this is not true: much of the energy at frequencies higher than the tenth baroclinic mode appears smooth in the frequency-wavenumber diagram shown in figure 5. The use of the tenth baroclinic mode works relatively well in our region A, but it is unlikely to be useful for partitioning the flow in regions with strong mesoscale currents. Although ω - k filtering is computationally cheaper than Lagrangian filtering, we do not think that it is applicable in all regions of the ocean.

We show that in region B, Lagrangian filtering preserves a lot of motions that appear superinertial in the reference frame of the Earth, but are subinertial in the reference frame of the flow. This is consistent with previous work by Callies et al. (2020), which showed that the velocity field observed at a fixed location in the North Atlantic is predominantly rotational even at apparently superinertial frequencies. Callies et al. (2020) hypothesized that they were observing balanced flow that was Doppler shifted into the superinertial range. In this paper we confirm that surface velocities in the superinertial range include Doppler-shifted motions, at least in the LLC4320 simulation.

In high-energy regions, Lagrangian filtering appears to be more likely to preserve flows close to filaments and fronts. It is likely that these flows are ageostrophically balanced. In realistic simulations (and in the ocean itself), there is not a clean metric to evaluate whether velocities are balanced, but we make use of the frontogenesis function and vorticity-strain JPDFs to understand the features of the velocities that are preserved by Lagrangian filtering. We show that it particularly preserves convergent flows in areas of frontogenesis. Preserving these convergent flows is likely to be important for modeling the vertical transport of ocean tracers. The differences between Lagrangian filtering and the other methods are larger in regions with high energy flows, like our region B, and smaller in regions without large-scale background flows, like our region A. More research is needed to identify when Lagrangian filtering is likely to be useful, and when it is an unnecessary computational expense.

Lagrangian filtering also removes motions that appear subinertial in the reference frame of the Earth, but are superinertial in the reference frame of the flow. This has not been observed before but consistent with the effects of Doppler shift hypothesized by Pinkel (2008). Because IGWs generally have lower energies than balanced motions, Doppler shifted IGWs do not have much effect on the total energy measured in the subinertial range.

We do not expect that the methods described here will be directly applied to SWOT observations. This paper represents the first step in the journey to extract the transport-relevant velocity field from high-resolution SSH observations. With these new insights about how to isolate balanced motions from the full velocity and SSH fields, we intend to create a large dataset that contains snapshots of filtered SSH, together with the filtered surface velocity field associated with each SSH snapshot. This dataset can then be used as a truth signal which can be used to define a supervised machine-learning problem for extracting the transport-relevant velocity field from low temporal resolution SSH snapshots. The method that is developed may then be applied to SWOT observations, finally leading to estimates ocean surface velocities.

This multistep process is involved, but has the potential to produce surface velocity data with high value to the scientific community. Alongside this approach, we advocate the use of intermediate approaches like using vorticity-strain joint PDFs (Balwada et al., 2021) to short-circuit directly to inference of transport-active flow from velocity, even with waves in latter.

5 Open Research

The code repository for this work is at <https://github.com/cspencerjones/separating-balanced>. The datasets used to create figures 3-7 are available at <https://doi.org/10.5281/zenodo.7495109> (Jones et al., 2022). Figures 1 and 2 can be created from the

603 LLC4320 data that is available via the pangeo catalog: [https://catalog.pangeo.io/
604 browse/master/ocean/LLC4320/](https://catalog.pangeo.io/browse/master/ocean/LLC4320/).

605 Acknowledgments

606 All authors acknowledge support from NASA award 80NSSC20K1142. This work would not
607 have been possible without the tools provided by and maintained by the Pangeo community
608 (<https://pangeo.io/>).

609 References

- 610 Abernathey, R. P., & Marshall, J. (2013). Global surface eddy diffusivities derived from
611 satellite altimetry. *Journal of Geophysical Research: Oceans*, *118*(2), 901–916.
- 612 Arbic, B. K., Elipot, S., Brasch, J. M., Menemenlis, D., Ponte, A. L., Shriver, J. F., ...
613 others (2022). Near-surface oceanic kinetic energy distributions from drifter obser-
614 vations and numerical models. *Journal of Geophysical Research: Oceans*, *127*(10),
615 e2022JC018551.
- 616 Balwada, D., Smith, K. S., & Abernathey, R. (2018). Submesoscale vertical velocities
617 enhance tracer subduction in an idealized antarctic circumpolar current. *Geophysical
618 Research Letters*, *45*(18), 9790–9802.
- 619 Balwada, D., Xiao, Q., Smith, S., Abernathey, R., & Gray, A. R. (2021). Vertical fluxes
620 conditioned on vorticity and strain reveal submesoscale ventilation. *Journal of Physical
621 Oceanography*.
- 622 Barton, A. D., Dutkiewicz, S., Flierl, G., Bragg, J., & Follows, M. J. (2010). Patterns of
623 diversity in marine phytoplankton. *Science*, *327*(5972), 1509–1511.
- 624 Brannigan, L., Marshall, D. P., Naveira-Garabato, A., & Nurser, A. G. (2015). The seasonal
625 cycle of submesoscale flows. *Ocean Modelling*, *92*, 69–84.
- 626 Bühler, O., Callies, J., & Ferrari, R. (2014). Wave–vortex decomposition of one-dimensional
627 ship-track data. *Journal of Fluid Mechanics*, *756*, 1007–1026.
- 628 Buijsman, M. C., Stephenson, G. R., Ansong, J. K., Arbic, B. K., Green, J. M., Rich-
629 man, J. G., ... Zhao, Z. (2020). On the interplay between horizontal resolution and
630 wave drag and their effect on tidal baroclinic mode waves in realistic global ocean
631 simulations. *Ocean Modelling*, *152*, 101656.
- 632 Callies, J., Barkan, R., & Garabato, A. N. (2020). Time scales of submesoscale flow inferred
633 from a mooring array. *Journal of Physical Oceanography*, *50*(4), 1065–1086.
- 634 Capet, X., McWilliams, J. C., Molemaker, M. J., & Shchepetkin, A. (2008). Mesoscale
635 to submesoscale transition in the california current system. part ii: Frontal processes.
636 *Journal of Physical Oceanography*, *38*(1), 44–64.
- 637 Caspar-Cohen, Z., Ponte, A., Lahaye, N., Carton, X., Yu, X., & Le Gentil, S. (2022).
638 Characterization of internal tide incoherence: Eulerian versus lagrangian perspectives.
639 *Journal of Physical Oceanography*.
- 640 Chouksey, M., Eden, C., & Brüggemann, N. (2018). Internal gravity wave emission in
641 different dynamical regimes. *Journal of Physical Oceanography*, *48*(8), 1709–1730.
- 642 Cronin, M. F., Gentemann, C. L., Edson, J., Ueki, I., Bourassa, M., Brown, S., ... others
643 (2019). Air-sea fluxes with a focus on heat and momentum. *Frontiers in Marine
644 Science*, 430.
- 645 Ducet, N., Le Traon, P.-Y., & Reverdin, G. (2000). Global high-resolution mapping of ocean
646 circulation from topex/poseidon and ers-1 and-2. *Journal of Geophysical Research:
647 Oceans*, *105*(C8), 19477–19498.
- 648 Eden, C., Chouksey, M., & Olbers, D. (2019). Gravity wave emission by shear instability.
649 *Journal of Physical Oceanography*, *49*(9), 2393–2406.
- 650 Egbert, G. D., Bennett, A. F., & Foreman, M. G. (1994). Topex/poseidon tides estimated
651 using a global inverse model. *Journal of Geophysical Research: Oceans*, *99*(C12),
652 24821–24852.

- 653 Egbert, G. D., & Erofeeva, S. Y. (2002). Efficient inverse modeling of barotropic ocean
654 tides. *Journal of Atmospheric and Oceanic Technology*, *19*(2), 183–204.
- 655 Elipot, S., Lumpkin, R., Perez, R. C., Lilly, J. M., Early, J. J., & Sykulski, A. M. (2016). A
656 global surface drifter data set at hourly resolution. *Journal of Geophysical Research:
657 Oceans*, *121*(5), 2937–2966.
- 658 Elipot, S., & Wenegrat, J. (2021). Vertical structure of near-surface currents—importance,
659 state of knowledge, and measurement challenges.
- 660 Ferrari, R. (2011). A frontal challenge for climate models. *Science*, *332*(6027), 316–317.
- 661 Furuichi, N., Hibiya, T., & Niwa, Y. (2008). Model-predicted distribution of wind-induced
662 internal wave energy in the world’s oceans. *Journal of Geophysical Research: Oceans*,
663 *113*(C9).
- 664 Grooms, I., Loose, N., Abernathey, R., Steinberg, J., Bachman, S. D., Marques, G.,
665 ... Yankovsky, E. (2021). Diffusion-based smoothers for spatial filtering of grid-
666 ded geophysical data. *Journal of Advances in Modeling Earth Systems*, *13*(9),
667 e2021MS002552.
- 668 Hoskins, B. J. (1982). The mathematical theory of frontogenesis. *Annual review of fluid
669 mechanics*, *14*(1), 131–151.
- 670 Jones, C. S., Xiao, Q., Abernathey, R. P., & Smith, K. S. (2022). *A dataset for comparing
671 filtering methods used to wave and non-wave flow at the surface of the agulhas region*
672 [dataset]. Zenodo. doi: 10.5281/zenodo.7495109
- 673 Kafiabad, H. A., & Bartello, P. (2016). Balance dynamics in rotating stratified turbulence.
674 *Journal of Fluid Mechanics*, *795*, 914–949.
- 675 Klein, P., Lapeyre, G., Siegelman, L., Qiu, B., Fu, L.-L., Torres, H., ... Le Gentil, S. (2019).
676 Ocean-scale interactions from space. *Earth and Space Science*, *6*(5), 795–817.
- 677 Lahaye, N., Gula, J., & Roulet, G. (2019). Sea surface signature of internal tides. *Geo-
678 physical Research Letters*, *46*(7), 3880–3890.
- 679 Lévy, M., Franks, P. J., & Smith, K. S. (2018). The role of submesoscale currents in
680 structuring marine ecosystems. *Nature communications*, *9*(1), 1–16.
- 681 Lilly, J. M., & Lettvin, E. (2004). The “switch-on” problem for linear time-invariant
682 operators. *Signal processing*, *84*(4), 763–784.
- 683 Luecke, C. A., Arbic, B. K., Richman, J. G., Shriver, J. F., Alford, M. H., Ansong, J. K.,
684 ... others (2020). Statistical comparisons of temperature variance and kinetic energy
685 in global ocean models and observations: Results from mesoscale to internal wave
686 frequencies. *Journal of Geophysical Research: Oceans*, *125*(5), e2019JC015306.
- 687 Mahadevan, A., Pascual, A., Rudnick, D. L., Ruiz, S., Tintoré, J., & D’Asaro, E. (2020).
688 Coherent pathways for vertical transport from the surface ocean to interior. *Bulletin
689 of the American Meteorological Society*, *101*(11), E1996–E2004.
- 690 Masur, G. T., & Oliver, M. (2020). Optimal balance for rotating shallow water in primitive
691 variables. *Geophysical & Astrophysical Fluid Dynamics*, *114*(4-5), 429–452.
- 692 Mazloff, M. R., Cornuelle, B., Gille, S. T., & Wang, J. (2020). The importance of remote
693 forcing for regional modeling of internal waves. *Journal of Geophysical Research:
694 Oceans*, *125*(2), e2019JC015623.
- 695 Mkhinini, N., Coimbra, A. L. S., Stegner, A., Arsouze, T., Taupier-Letage, I., & Béranger,
696 K. (2014). Long-lived mesoscale eddies in the eastern mediterranean sea: Analysis
697 of 20 years of aviso geostrophic velocities. *Journal of Geophysical Research: Oceans*,
698 *119*(12), 8603–8626.
- 699 Morrow, R., Fu, L.-L., Ardhuin, F., Benkiran, M., Chapron, B., Cosme, E., ... others
700 (2019). Global observations of fine-scale ocean surface topography with the surface
701 water and ocean topography (swot) mission. *Frontiers in Marine Science*, *6*, 232.
- 702 Niiler, P., Maximenko, N., Pantelev, G., Yamagata, T., & Olson, D. (2003). Near-surface
703 dynamical structure of the kuroshio extension. *Journal of Geophysical Research:
704 Oceans*, *108*(C6).
- 705 Onuki, Y. (2020). Quasi-local method of wave decomposition in a slowly varying medium.
706 *Journal of Fluid Mechanics*, *883*.

- 707 Pinkel, R. (2008). Advection, phase distortion, and the frequency spectrum of finescale
708 fields in the sea. *Journal of physical oceanography*, *38*(2), 291–313.
- 709 Plumb, R. (1979). Eddy fluxes of conserved quantities by small-amplitude waves. *Journal*
710 *of atmospheric sciences*, *36*(9), 1699–1704.
- 711 Ponte, A. L., Klein, P., Dunphy, M., & Le Gentil, S. (2017). Low-mode internal tides and
712 balanced dynamics disentanglement in altimetric observations: Synergy with surface
713 density observations. *Journal of Geophysical Research: Oceans*, *122*(3), 2143–2155.
- 714 Qiu, B., Chen, S., Klein, P., Torres, H., Wang, J., Fu, L.-L., & Menemenlis, D. (2020). Re-
715 constructing upper-ocean vertical velocity field from sea surface height in the presence
716 of unbalanced motion. *Journal of Physical Oceanography*, *50*(1), 55–79.
- 717 Resplandy, L., Lévy, M., Madec, G., Pous, S., Aumont, O., & Kumar, D. (2011). Con-
718 tribution of mesoscale processes to nutrient budgets in the arabian sea. *Journal of*
719 *Geophysical Research: Oceans*, *116*(C11).
- 720 Richman, J. G., Arbic, B. K., Shriver, J. F., Metzger, E. J., & Wallcraft, A. J. (2012).
721 Inferring dynamics from the wavenumber spectra of an eddying global ocean model
722 with embedded tides. *Journal of Geophysical Research: Oceans*, *117*(C12).
- 723 Rocha, C. B., Gille, S. T., Chereskin, T. K., & Menemenlis, D. (2016). Seasonality of sub-
724 mesoscale dynamics in the kuroshio extension. *Geophysical Research Letters*, *43*(21),
725 11–304.
- 726 Savage, A. C., Arbic, B. K., Alford, M. H., Ansong, J. K., Farrar, J. T., Menemenlis, D.,
727 ... others (2017). Spectral decomposition of internal gravity wave sea surface height
728 in global models. *Journal of Geophysical Research: Oceans*, *122*(10), 7803–7821.
- 729 Shakespeare, C. J., Gibson, A. H., Hogg, A. M., Bachman, S. D., Keating, S. R., & Velze-
730 boer, N. (2021). A new open source implementation of lagrangian filtering: A method
731 to identify internal waves in high-resolution simulations. *Journal of Advances in Mod-*
732 *eling Earth Systems*, *13*(10), e2021MS002616.
- 733 Shakespeare, C. J., & Hogg, A. M. (2017). Spontaneous surface generation and interior
734 amplification of internal waves in a regional-scale ocean model. *Journal of Physical*
735 *Oceanography*, *47*(4), 811–826.
- 736 Sinha, A., Balwada, D., Tarshish, N., & Abernathey, R. (2019). Modulation of lateral
737 transport by submesoscale flows and inertia-gravity waves. *Journal of Advances in*
738 *Modeling Earth Systems*, *11*(4), 1039–1065.
- 739 Stammer, D., Ray, R., Andersen, O. B., Arbic, B., Bosch, W., Carrère, L., ... others (2014).
740 Accuracy assessment of global barotropic ocean tide models. *Reviews of Geophysics*,
741 *52*(3), 243–282.
- 742 Torres, H. S., Klein, P., Menemenlis, D., Qiu, B., Su, Z., Wang, J., ... Fu, L.-L. (2018).
743 Partitioning ocean motions into balanced motions and internal gravity waves: A mod-
744 eling study in anticipation of future space missions. *Journal of Geophysical Research:*
745 *Oceans*, *123*(11), 8084–8105.
- 746 Uchida, T., Balwada, D., P Abernathey, R., A McKinley, G., K Smith, S., & Lévy, M.
747 (2020). Vertical eddy iron fluxes support primary production in the open southern
748 ocean. *Nature communications*, *11*(1), 1–8.
- 749 Van Sebille, E., Aliani, S., Law, K. L., Maximenko, N., Alsina, J. M., Bagaev, A., ...
750 others (2020). The physical oceanography of the transport of floating marine debris.
751 *Environmental Research Letters*, *15*(2), 023003.
- 752 Viúdez, Á., & Dritschel, D. G. (2004). Optimal potential vorticity balance of geophysical
753 flows. *Journal of Fluid Mechanics*, *521*, 343–352.
- 754 Wang, J., Fu, L.-L., Qiu, B., Menemenlis, D., Farrar, J. T., Chao, Y., ... Flexas, M. M.
755 (2018). An observing system simulation experiment for the calibration and validation
756 of the surface water ocean topography sea surface height measurement using in situ
757 platforms. *Journal of Atmospheric and Oceanic Technology*, *35*(2), 281–297.
- 758 Yu, X., Ponte, A. L., Elipot, S., Menemenlis, D., Zaron, E. D., & Abernathey, R. (2019).
759 Surface kinetic energy distributions in the global oceans from a high-resolution nu-
760 merical model and surface drifter observations. *Geophysical Research Letters*, *46*(16),
761 9757–9766.

- 762 Yu, X., Ponte, A. L., Lahaye, N., Caspar-Cohen, Z., & Menemenlis, D. (2021). Geostrophy
763 assessment and momentum balance of the global oceans in a tide-and eddy-resolving
764 model. *Journal of Geophysical Research: Oceans*, *126*(10), e2021JC017422.
- 765 Zaron, E. D., & Rocha, C. B. (2018). Internal gravity waves and meso/submesoscale currents
766 in the ocean: anticipating high-resolution observations from the swot swath altimeter
767 mission. *Bulletin of the American Meteorological Society*, *99*(9), ES155–ES157.
- 768 Zhao, Z., Wang, J., Menemenlis, D., Fu, L.-L., Chen, S., & Qiu, B. (2019). Decomposition
769 of the multimodal multidirectional m2 internal tide field. *Journal of Atmospheric and*
770 *Oceanic Technology*, *36*(6), 1157–1173.